



**HAL**  
open science

## **Evolution of the off-fault deformation of strike-slip faults in a sand-box experiment**

Sarah Visage, Pauline Souloumiac, Nadaya Cubas, Bertrand Maillot, Solene Antoine, Arthur Delorme, Yann Klinger

### ► **To cite this version:**

Sarah Visage, Pauline Souloumiac, Nadaya Cubas, Bertrand Maillot, Solene Antoine, et al. Evolution of the off-fault deformation of strike-slip faults in a sand-box experiment. *Tectonophysics*, 2023, 847, <10.1016/j.tecto.2023.229704>. <insu-03947005>

**HAL Id: insu-03947005**

**<https://insu.hal.science/insu-03947005v1>**

Submitted on 31 Mar 2025

**HAL** is a multi-disciplinary open access archive for the deposit and dissemination of scientific research documents, whether they are published or not. The documents may come from teaching and research institutions in France or abroad, or from public or private research centers.

L'archive ouverte pluridisciplinaire **HAL**, est destinée au dépôt et à la diffusion de documents scientifiques de niveau recherche, publiés ou non, émanant des établissements d'enseignement et de recherche français ou étrangers, des laboratoires publics ou privés.



Distributed under a Creative Commons CC BY-NC 4.0 - Attribution - Non-commercial use - International License



Contents lists available at ScienceDirect

## Tectonophysics

journal homepage: [www.elsevier.com/locate/tecto](http://www.elsevier.com/locate/tecto)



# Evolution of the off-fault deformation of strike-slip faults in a sand-box experiment

Sarah Visage<sup>a,\*</sup>, Pauline Souloumiac<sup>a</sup>, Nadaya Cubas<sup>b</sup>, Bertrand Maillot<sup>a</sup>, Solene Antoine<sup>c</sup>, Arthur Delorme<sup>c</sup>, Yann Klinger<sup>c</sup>

<sup>a</sup> Laboratoire Géosciences et Environnement Cergy, CY Cergy Paris Université, France

<sup>b</sup> Sorbonne Université, CNRS-INSU, Institut des Sciences de la Terre Paris, ISTeP UMR 7193, F-75005 Paris, France

<sup>c</sup> Institut de Physique du Globe de Paris, Université de Paris, CNRS, 75238 Paris, France

### ARTICLE INFO

#### Keywords:

Strike-slip fault  
Off-fault deformation  
Analogue modelling  
Optical image correlation

### ABSTRACT

Surface deformation associated with strike-slip faults can be distributed in space, with deformation located either along the primary fault strand or around it and referred to as off-fault deformation (OFD). Fault displacement hazard evaluation require to identify and estimate surface slip rates along active fault strands. We calculate the horizontal and vertical displacement of the analogue models surfaces with optical image correlation and photogrammetry, to investigate the OFD's development with increasing cumulative deformation. The criterion uses the gradient of the horizontal displacement norm perpendicular to the basal fault. Below 0.005 (noise level), there is no deformation, up to 0.03, it is off-fault-deformation, above 0.03, it is on-fault. We confirm previous observations made on analogue models that the surface deformation starts with a broad diffuse deformation, then produces fault strands alternating with relay zones that may be abandoned and reactivated. OFD is located first between Riedels, then between synthetic shears, and finally takes place in the relay zones. We also show that the OFD initially accommodates 100% of the applied slip (no faults), then decreases abruptly during the Riedels stage down to 20 to 30% to finally remain stable for the rest of the experiment. The abandonment and reactivation of the relay zones has the consequence of maintaining the OFD ratio on a stable value. Our experiments show that, like the OFD ratio, the width of the fault zone decreases with cumulative displacement to reach a stable value. Consequently, the OFD is correlated with this fault zone width and its geometric complexities. The ratios of OFD observed in this study are also consistent with measurements of OFD made on seven natural faults that exhibit different cumulative displacements. Hence our models suggest that strike-slip faults will never reach a continuous, linear geometry, and will always maintain a minimum amount of OFD.

## 1. Introduction

During a strike-slip rupture, the surface deformation is partly accommodated by the main fault strands, and partly distributed over hundreds of meters from the main fault strands. This off-fault deformation (OFD) takes the form of secondary faults and fractures, shears, rotations, and other processes resulting in permanent bending and warping (e.g., McGill and Rubin, 1999; Shelef and Oskin, 2010). The identification of active fault strands, and the quantification of their surface slip rates are primary inputs for probabilistic fault displacement hazard models, earthquakes forecasting, and dynamic models studying the interaction between the OFD and earthquake mechanics (e.g., Dunham et al., 2011; Gabriel et al., 2013; Thomas and Bhat, 2018; Baize

et al., 2020; Klinger et al., 2018). Yet, the understanding of surface slip rates requires constraining the on- to off-fault deformation ratio.

According to field studies, the off-fault deformation along continental strike-slip faults is highly variable, some surface ruptures being fully accommodated by the main fault strands while others are completely distributed (e.g., Dolan and Haravitch, 2014 and references therein). Recent advances in satellite imagery have overcome the difficulty faced by field studies in providing a complete picture of the distribution of the off-fault deformation over the entire rupture path up to hundreds of meters around it (Gold et al., 2015; Milliner et al., 2015, 2016; Vallage, 2016; Klinger et al., 2018; Antoine et al., 2021; Choi et al., 2018). These studies have shown that, to the first order, the distribution of OFD is strongly correlated to the structural complexities, or

\* Corresponding author.

E-mail address: [sarah.visage@cyu.fr](mailto:sarah.visage@cyu.fr) (S. Visage).

<https://doi.org/10.1016/j.tecto.2023.229704>

Received 22 July 2022; Received in revised form 28 December 2022; Accepted 31 December 2022

Available online 5 January 2023

0040-1951/© 2023 Published by Elsevier B.V.

geometrical irregularities, of the main fault strands (e.g., Zinke et al., 2014; Milliner et al., 2015; Gold et al., 2015; Vallage, 2016; Antoine et al., 2021). Strike slip faults are indeed formed by a succession of fault strands, possibly bent, separated by relay zones (e.g., Segall and Pollard, 1980). The OFD increases notably along those complexities which are also known to affect the initiation, propagation and the arrest of earthquakes (e.g., King and Nábělek, 1985; Klinger et al., 2005; Wesnousky, 2006; Manighetti et al., 2007). These complexities are partly related to some structural inheritance, from old structures formed from different kinematics then reactivated during the formation of the strike-slip fault. However, inheritance will not be addressed in this study.

From the comparison of different events, some studies have also confirmed that the OFD ratio varies with the cumulative slip on the fault, with values above 50% for relatively immature faults down to about 18–20% for faults with a large displacement (Dolan and Haravitch, 2014; Klinger et al., 2006).

These large differences, along a single fault and between different faults prevent us from applying a fixed ratio of OFD to quantify surface slip rates and call for a better understanding of the parameters controlling the OFD distribution. Moreover, seismic ruptures are too scarce for reliable statistical analysis, not to mention the difficulties related to the diversity of OFD definitions and measurement techniques, and the distinction of elastic and inelastic deformation.

To understand the origin, the distribution, and the evolution of the OFD along a strike-slip fault, here we use analogue models. Previous analogue modelling studies have led to the identification of several formation stages from the *en-échelon* Riedel shears to the anastomosed fault (e.g. Tchalenko, 1970; Hatem et al., 2017; Lefevre et al., 2020; Dooley and Schreurs, 2012; Riedel, 1929). Our work builds on these results, and aims at providing a precise quantification and an understanding of the evolution of the OFD along the fault zone and throughout these different stages. We here use sand as an analogue of the crustal

material. Due to the essentially plastic behavior of the sand (it is too rigid to accumulate measurable elastic deformation), our study will provide reports on the OFD inherent in the fault zone structure without the elastic deformation component.

In the following, we first describe our experimental set-up, the optical image correlation method and our chosen off-fault deformation criterion. We then detail the results, starting with a description of the different stages of formation of strike-slip faults, followed by the distribution, quantification, and a 3D description of the on- and off-fault deformation during the evolution of strike-slip faults. We finally discuss the impact of the initial diffuse deformation zone on the fault zone history and summarize the control of inherited structures on the distribution of the off-fault deformation of strike-slip faults.

## 2. Methods

### 2.1. Experimental setup

The experimental device is composed of two juxtaposed PVC plates of 1500 mm × 670 mm each, simulating a straight vertical basement fault. One plate is fixed while the other one is pushed forward by a motor, generating a sinistral strike-slip deformation in the overlying material (Fig. 1). The width of the box is large enough to avoid any edge effect following the work done by Lefevre et al. (2020). The surface deformation is recorded by four cameras placed one meter above the sandbox: three of them form a triangle, the fourth in the center of the triangle pointing to the center of the sandbox surface (Fig. 1). Cameras angles were chosen to obtain the vertical displacement of the surface. Cameras are Nikon D3200 with a 18 mm lens. Each picture covers a surface of 1030 mm × 680 mm, resulting in a resolution of 0.18 mm per pixel. The pictures are taken every 0.5 mm of displacement.

We used a Fontainebleau aeolian quartz sand (named CV32),

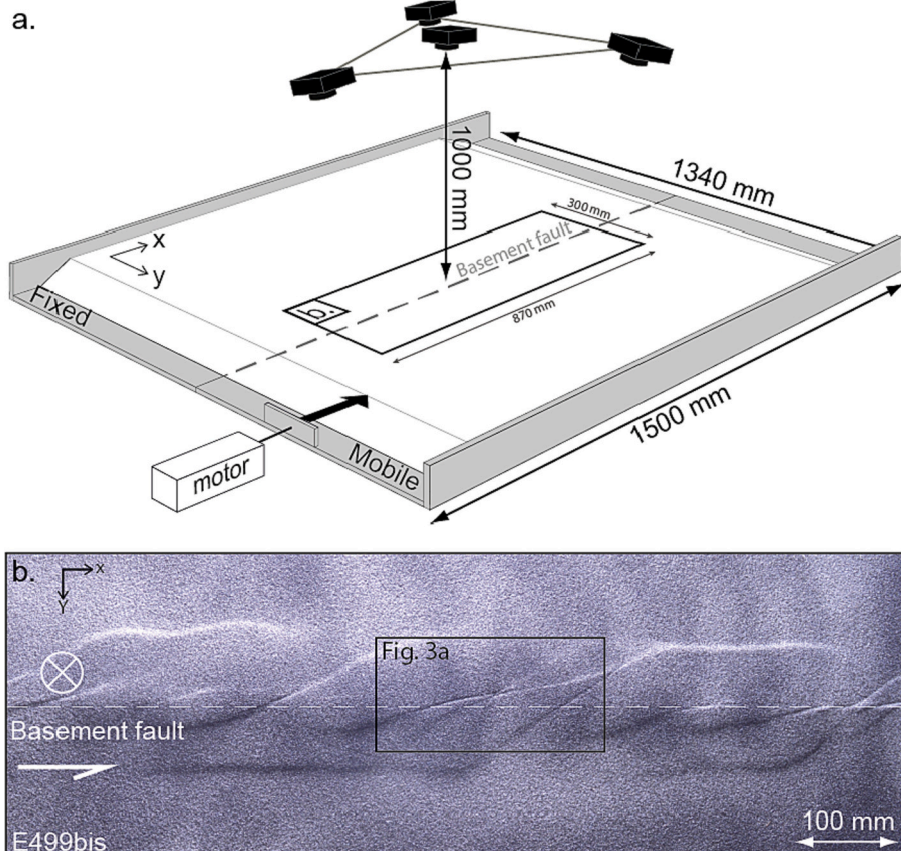


**Fig. 1.** (a) Strike-slip fault experimental setup. The box consists of two rigid PVC plates: one is fixed, the other is pushed forward by a motor, to simulate a sinistral strike-slip basal fault. Both plates are covered with a single flat sand pack of various thicknesses and densities. Experiments are recorded by four cameras placed on top of the material. (b) Example topview photography of the sand surface after 25 mm of displacement with oblique lighting coming from the top part. The dashed line indicates the location of the basal fault.

composed of 98% quartz, with an median grain size of 250  $\mu\text{m}$ . The sand pack was either sedimented with a sand distributor (Maillot, 2013) or deposited manually, by 2 cm increments smoothed with a squeegee to obtain a flat surface. The sedimented sand has a static internal friction angle of 43.7°, a dynamic friction of 35.9°, and a density of 1711  $\pm$  7  $\text{kg}/\text{m}^3$ . The poured sand (manually deposited) has a static internal friction of 33.4°, a dynamic friction of 34.2°, and a density of 1680  $\text{kg}/\text{m}^3$  with an unknown uncertainty due to the manual mode of deposit (Maillot, 2013; Cubas et al., 2010; Klinkmüller et al., 2016; Lefevre et al., 2020). Temperature (between 18 and 25 °C) and humidity (between 45 and 55%) of the laboratory are monitored to avoid large variations that could affect the sand properties.

We performed a total of twenty experiments. We varied the thickness from 20 to 80 mm. To evaluate the effect of the internal friction value, we used both poured and sedimented sands. The applied displacement ranges from 50 to 150 mm, as summarized in Table 1.

The deformation of dry sand is not sensitive to the rate of the applied displacement, therefore, there is no specific time scale in our experiments. The sand has a very low cohesion therefore we did not use it to set a length scale (Maillot, 2013). Consequently, the thickness of the sand pack corresponds to the thickness of the frictional part of the crust. Here, we set thicknesses between 40 and 80 mm that correspond to 8 to 16 km in nature, if we set the length scale  $L^* = 0.5 \times 10^{-5}$  (with  $L^* = \frac{L_{\text{model}}}{L_{\text{nature}}}$ ).

## 2.2. Optical image correlation

We used optical image correlation, via the free, open-source photogrammetry software MicMac (Rosu et al., 2015; Rupnik et al., 2017; Galland et al., 2016) to calculate the horizontal and vertical deformation of the experiment surface. The horizontal displacement field was obtained by correlating the raw images (i.e. without any geometric corrections) acquired by the camera placed at the center of the triangle pointing to the sandbox center. The principle of image correlation is to match a group of pixels (9\*9 px in our case) between two images (Rosu et al., 2015). From the horizontal displacement field, we calculate the displacement norm, which represents the amplitude of displacement (Fig. 2-a):

$$U = \sqrt{U_x^2 + U_y^2}, \quad (1)$$

the divergence which represents the dilatancy and contraction (Fig. 2-c):

$$\frac{\partial U_x}{\partial x} + \frac{\partial U_y}{\partial y}, \quad (2)$$

the curl which represents the deformation in clockwise and anticlockwise rotation (Fig. 2-d):

**Table 1**  
Experiment number and experimental parameters.

Experiment Nr	Sand thickness [mm]	Total displacement [mm]	Type of deposit
E439, E440	40	50	Poured
E448 to E450	80	50	Poured
E451	60	50	Poured
E453	50	50	Poured
E455, E456	70	50	Poured
E457	50	50	Poured
E458	50	50	Sedimented
E461	60	50	Sedimented
E464	70	75	Sedimented
E466	80	100	Sedimented
E481 to E484, E494	60	150	Poured
E499, E499bis	60	150	Sedimented

$$\frac{\partial U_y}{\partial x} - \frac{\partial U_x}{\partial y}, \quad (3)$$

and the on- and off-fault deformation map from the criterion defined in the next paragraph (Fig. 2-b). The vertical displacement (which represents the uplift) at the surface is obtained using the four cameras, simultaneously triggered. We first calculate the digital surface model (DSM) for each displacement step (Fig. 2-f). Then we subtract the DSMs from two displacement steps, taking into account the horizontal displacement field, to compute the vertical displacement field (Delorme et al., 2020) (Fig. 2-e). All results were co-registered using targets with known 3D coordinates (ground control points, GCPs) laid out on the surface (Galland et al., 2016).

The calculations of the horizontal displacement were performed independently of the vertical displacement. Therefore the images were orthorectified for the vertical displacement calculation but not for the horizontal displacement, because the only camera used is placed above the experiment with a view angle perpendicular to the sand surface. Furthermore, we did not correct the distortion of the pictures because the difference between distorted and undistorted pictures is negligible (see Fig.S9 on the Supplements).

## 2.3. Off-fault deformation criterion

In our models, we consider that we are in the fault zone when we are above the noise level on the second invariant of the strain tensor (see Fig.S2 on Supplements):

$$I_2 \geq 0.00136 \quad (4)$$

In this fault zone, on-and off-fault deformation is present, and we define the OFD ratio as the percentage of the total displacement that is not accommodated by the faults. To automatically calculate this OFD ratio, we need an automated way to measure the displacement occurring on the faults, and hence, an automatic criterion to detect the on-fault deformation. This criterion is illustrated with the help of Fig. 3-a that shows the displacement norm issued from the optical image correlation for an increment between two photos of 0.5 mm. On the fixed part of the box the displacement of the sand is zero (blue area) and on the moving part of the box the displacement of the sand is 0.5 mm (red area). After analysis of the horizontal displacement field calculated with image correlation and of several profiles of the displacement norm across the fault zone described in the Supplements (see Figs.S3 and S4), we decided to consider that there is an active fault wherever:

$$\left| \frac{\partial U}{\partial y} \right| \geq 0.03. \quad (5)$$

This gradient perpendicular to the fault is calculated by finite-differences (central differences, taking one point out of ten in order to limit noise) and is illustrated by the red patches in Fig. 3b.

$$\frac{\partial U}{\partial y}(y) = \frac{U(y - 10dy) - U(y + 10dy)}{20dy}. \quad (6)$$

Where  $dy = 0.18$  mm is the pixel size. Next, the OFD ratio is calculated for each profile (Fig. 3c). According to this criterion, the blue profile crossing a Riedel shear has an OFD ratio of 22.8 + 14 = 36.8% of the applied far field displacement of 0.5 mm, while the red profile crossing an inter-Riedel zone has an OFD ratio of 55.3 + 17.4 = 72.7%. Note that in doing this calculation, we set the gradient to zero at any point where

$$\left| \frac{\partial U}{\partial y} \right| \leq 0.005, \quad (7)$$

which is the magnitude of the noise of the horizontal displacement field as determined in the Supplements (see Fig.S1). At points where the

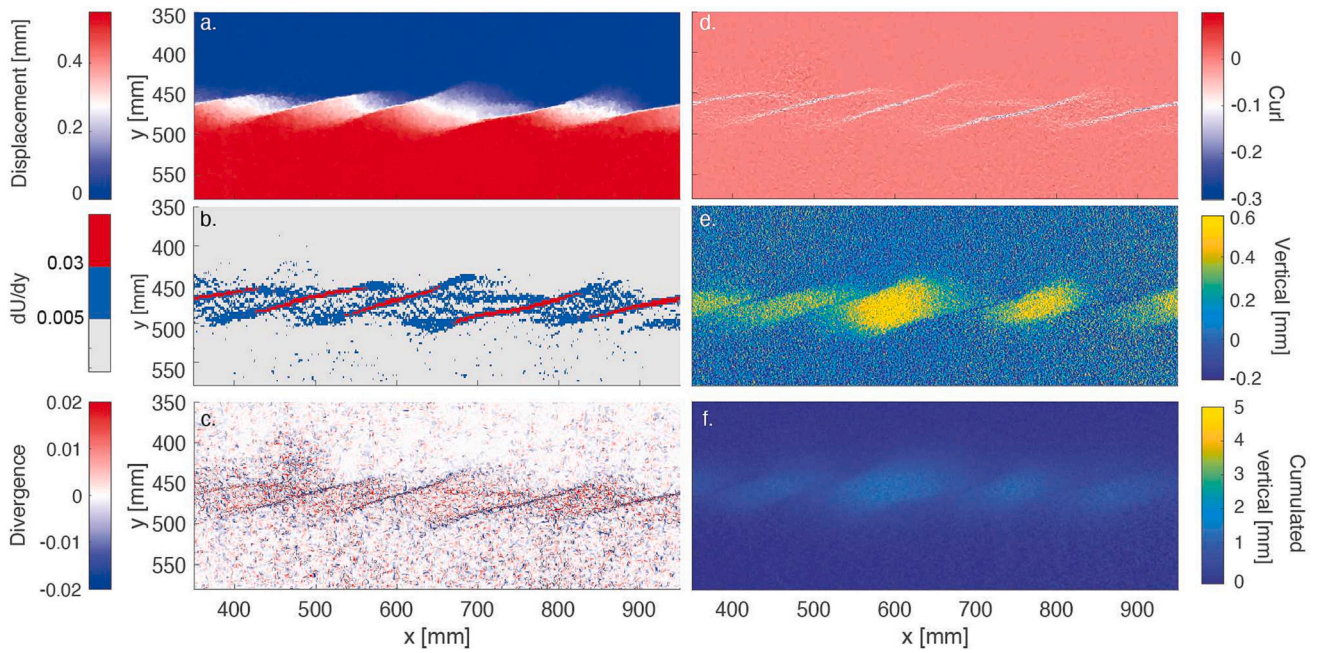
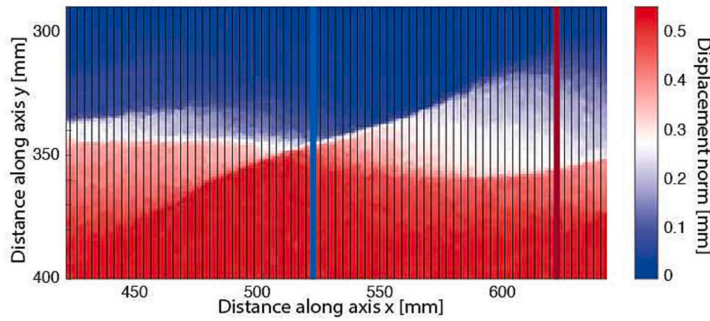
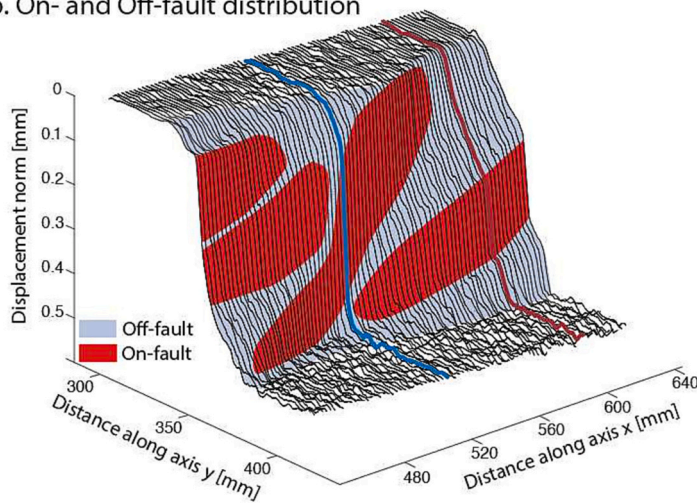


Fig. 2. Optical image correlation results from experiment E494 at 9 mm cumulative displacement. (a) Horizontal displacement norm. (b) On- and off-fault deformation map. (c) Divergence. (d) Curl. (e) Cumulative uplift between 8.5 and 10.5 mm. (f) Cumulative uplift.

a. Norm of displacement



b. On- and Off-fault distribution



c. Off-fault ratio quantification

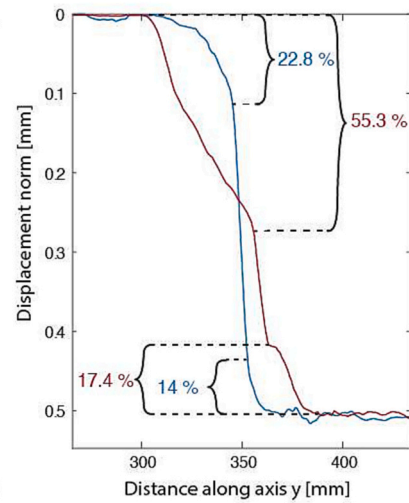


Fig. 3. Definition of the OFD criterion. (a) Horizontal displacement norm of a zoom on experiment E481 after 10 mm of applied displacement. OFD ratios are calculated all over the box along regularly spaced profiles perpendicular to the basal fault. The red profile is located along a future fault strands; the blue profile crosses a Riedel shear. (b) 3D view of the displacement profiles which shows the spatial distribution of the on-fault (red area) and off-fault (blue area) displacement. (c) Horizontal displacement norms for blue and red profiles with ratios of the OFD associated to each profile.

criterion (Eq. 7) is met, we consider that the OFD is zero.

Finally, the OFD ratio for the entire study area is the average value of the ratios of each profile perpendicular to the basal fault.

### 3. Results

#### 3.1. Stages of strike-slip fault formation

We describe the four major stages of the formation of a strike-slip fault zone in our experiments, that have already been thoroughly described in the literature (Tchalenko, 1970; Naylor et al., 1986; Hatem et al., 2017; Jiao et al., 2021). In order to illustrate the different stages of the fault zone formation, we carried out an experiment with grazing light and sedimented sand, which allows the structures to be clearly seen in the photos (E499bis, Fig. 4). The sedimented sand has a high density, the maximum it can achieve (see Maillot, 2013), so in the experiment the pack needs more expansion, than with deposited sand, to start localising deformation in shear bands. Therefore, the structures are more visible at the surface of the sand pack. The initiation stage is characterized by diffuse deformation and an uplift above the basal fault (Fig. 4-a). The width of this zone, perpendicular to the basal fault, varies

with the thickness of the sand pack (the thicker the sand pack the wider the diffuse deformation zone, Lefevre et al., 2020). After about 4 to 8 mm of displacement, the deformation localizes along *en échelon* shears called Riedels (Fig. 4-b). The Riedels strike at an angle of  $\frac{\phi}{2}$  to the basal fault (with  $\phi$  the internal friction angle of the sand). The Riedels length and the spacing also vary with the thickness of the sand pack (the thicker the sand pack the longer and more distant the Riedels are, Lefevre et al., 2020). At the beginning of the strike-slip fault activity, two fault planes form from the basal fault and reach the surface on both sides of the future fault zone, these faults have mostly a reverse component accommodating the uplift along the basal fault. When the Riedels form, they merge on these two fault planes. However, we can only observe them with sedimented sand, due to the high density of the sand pack and thus a higher dilatancy. When the sand is poured, they do not reach the surface of the model. R' shears, conjugate segments of the Riedel shears, do not develop in our experiments. We have no explanation for the absence of R' faults. Dooley and Schreurs (2012) show that in sand R' are rarely visible, but that they can be observed in clay, however no mechanical explanation is proposed.

In the following stage (interaction stage), synthetic shears, striking at

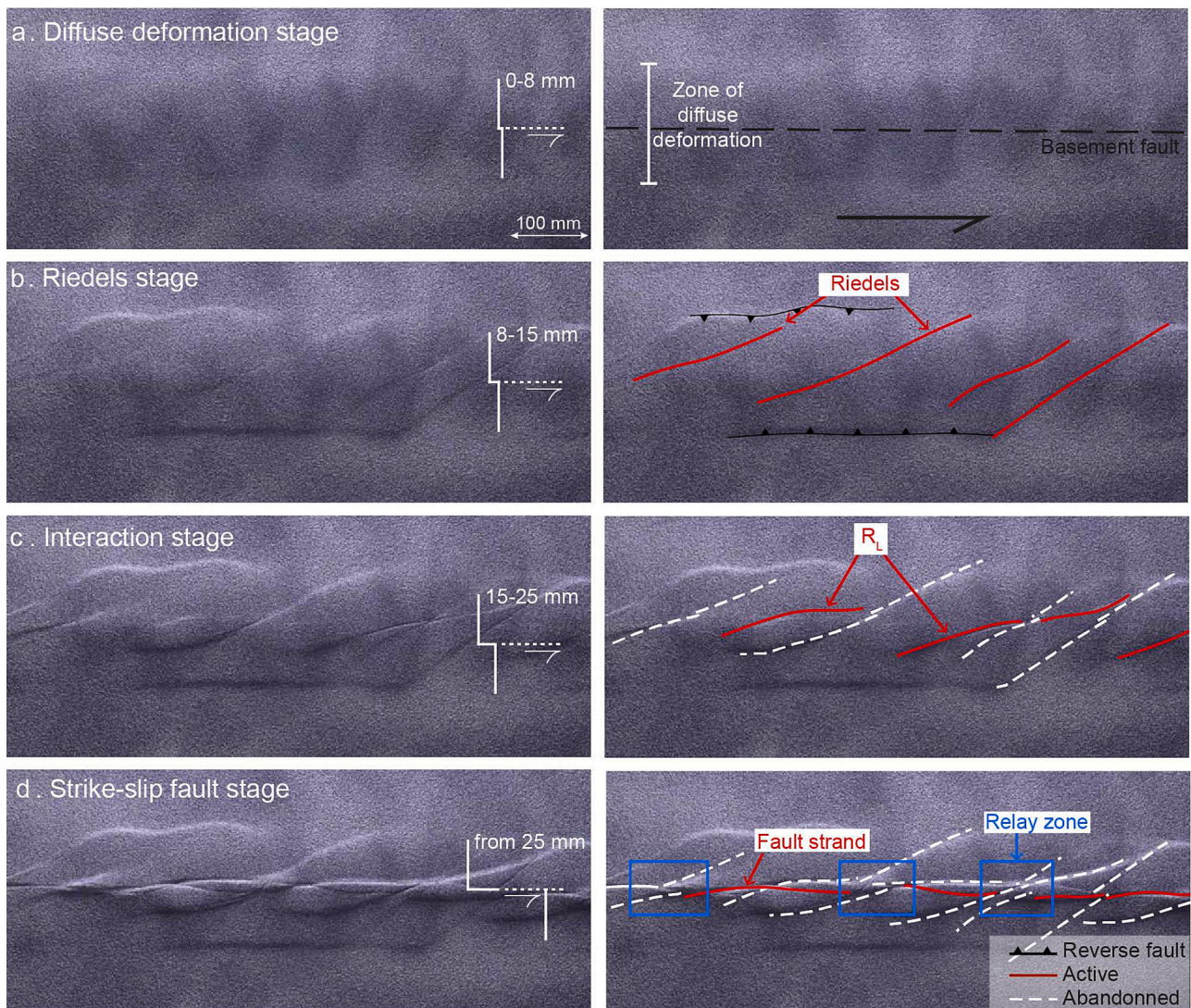


**Fig. 4.** Surface photographs of the stages of the formation of an analogue strike-slip fault with oblique lighting coming from the top left, in a 60 mm thick sedimented sand (E499bis). Left column: raw photos, right column: interpreted photos. (a) Diffuse deformation stage, (b) Riedels stage, (c) Interaction stage, (d) Strike-slip fault stage where the fault zone is formed of fault strands separated by relay zones (blue rectangles) located along abandoned Riedels. Red solid lines indicate active faults while white dashed lines indicate inactive faults.

a smaller angle to the basal fault than the Riedels (about  $\frac{1}{2}$ ), emerge in between the Riedels (Fig. 4-c). These structures are referred to as  $R_L$  (Schreurs, 2003). These shear structures then coalesce to form an anastomosed fault zone (Fig. 4-d).

The strike-slip fault stage lasts from 25 mm of cumulative displacement until the end of the experiment. At this stage, the fault zone is formed of complexities, where the fault is not continuous and/or composed of several parallel strands called relay zones, which alternate with sections with a single and continuous fault strand.

### 3.2. Distribution of on- and off-fault deformation during the strike-slip fault formation

We now describe in detail the evolution of the OFD location, as well as the evolution of the OFD ratio and of the active shear zone width for experiment E494 with a 60 mm thick sand pack, from the beginning up to 139 mm of cumulative displacement (Fig. 5). We chose to describe experiment E494 because it illustrates all the findings of this study. The evolution for experiments E481, E482, E483 and E484 with 60 mm of thickness are provided in the Supplements. The Fig. 5-a is obtained from a map of the distribution of on- and off-fault deformation (based on the criteria (5) and (7), Figs. 2-b and 3). The width of the active shear zone (Fig. 5-b) is automatically obtained for each increment by analyzing the area where the second invariant of the strain tensor is above the noise level (see the Supplements). As described above, a broad zone of a diffuse deformation of 74 mm wide first forms on the surface of the model. Hence, during the diffused deformation stage, the OFD accounts for 100% of the deformation at the model surface. After 7.5 mm of cumulative displacement, Riedels appear on the surface and OFD areas concentrate between these Riedels. The OFD is still predominant (65%) and the width of the active shear zone is 66 mm. The interaction stage is reached at 13.5 mm of cumulative displacement. Shear bands ( $R_L$ ) develop between the Riedels and interact with them. Some OFD remains between the different shears, and the OFD ratio (41%) drops as shears develop. The width of the active shear zone is now 55 mm. At 18.5 mm of cumulative displacement, the Riedels are progressively abandoned. The shear bands partly extend along the abandoned Riedels, and parallel the basal fault to form the future fault strands. Former Riedels are now sheared and will form the future relay zones. The OFD is located in the relay zones and the OFD ratio decreases (26%). At this stage, the width of the active shear zone is 52 mm.

At 33.5 mm of cumulative displacement, fault strands are parallel to the basal fault and still end where former Riedels are sheared. The relay zones in the grey rectangles acquire more complexity. The OFD is concentrated in these relay zones but also along some fault strands (20%) and the width of the active shear zone decreases to 47 mm. This alternation of fault strands (single fault strand parallel to the basal fault) and relay zones (structurally complex with OFD) marks the beginning of the fault stage. The fault strand length is of the order of the inter-Riedel distance. At this stage, we identify four relay zones, separated by fault strands which length are on average 2.9 times the thickness of the sand (the length of a fault strand is measured between the two ends of the strand, as represented by the green dashed lines in Fig. 9). At 46 mm of cumulative displacement, the relay zone of Riedel R2 is abandoned, doubling the length of the fault strand now extending from R1 to R3 (5.7 times the sand thickness). The width of the shear zone and the OFD ratio decrease to reach here their minimum value: 43 mm and 19%.

At 58.5 mm of cumulative displacement, a new relay zone is formed between Riedels R2 and R3 (green box), at the location of a former shear zone whose activity was abandoned between 18.5 mm and 46 mm and was characterized by residual OFD. All fault strands recover to near their initial length, which in this case is about 2.83 times the material thickness. The width of the shear zone increases to 47 mm. The OFD ratio is always found in the relay zone, as well as along the old structures, and, like the width of the shear zone, increases to 24%. Between

58.5 and 71 mm of cumulative displacement, the relay zone on R3 is abandoned and the new relay zone (green box) is transported with the fault activity to the location of the former Riedel R3. Between 95 and 118 mm of cumulative displacement, the relay zones on R3 and R4 propagate and merge to form a long relay zone (blue box). The fault strand between R1 and R3 then reaches 7.5 times the sand thickness. At this stage, the OFD is located all along the fault zone and the width of the active shear zone is still 48 mm. Finally, at 139 mm of cumulative displacement, the former R1-R3 fault strand is again separated by a new relay zone, formed at the intersection with the former R2 (green box).

During each fault stage, relay zones constantly evolve. They are first sheared, then abandoned, passively translated, sometimes reactivated when crossing former shear bands. OFD reaches a minimum at the beginning of the fault stage of 19% and then increases to a stable value of 24–28% maintained until the end of the experiment. And so the same consequence is observed for the width of the active shear zone which decreases to a minimum at 43 mm and then increases to a stable value of 48 mm and remains constant until the end of the experiment. The same evolution is observed in all the experiments carried out within the framework of this study and a precise description of four other experiments with similar parameters (E481 to E484, Table 1) is presented in the Supplements (see Figs. S5 to S8).

### 3.3. Quantification of the off-fault deformation during the formation of the strike-slip fault

To measure the evolution of OFD with increasing cumulative fault displacement, we use fixed profiles across the experiment where the OFD ratio is calculated at each time increment throughout the experiment. We place the first profile between two up-coming Riedels, that will eventually cross a fault strand (Fig. 6). The second one is located across a future Riedel shear that will evolve as a relay zone (Fig. 7). The OFD ratio is determined according to the criterion defined in Section 2.3. All quoted percentages are from the red moving averages provided in Figs. 6 and 7.

At the initiation stage, for both cases, the OFD ratio is 100%, and corresponds to the diffuse deformation zone (inset 1 of Figs. 6 and 7). This proportion then decreases strongly from 100% to 32% (inset 2, Fig. 6) and 35% (inset 2, Fig. 7) during the formation of the Riedel shears.

For the profile located across what will become a fault strand (Fig. 6), the OFD ratio continues to decrease during the formation of the  $R_L$  shears (interaction stage, green zone in Fig. 6), with values ranging between 25 and 15%. At the fault stage, the OFD ratio reaches stable value between 22% and 8% with an average of 14.5% (14.5% at 60 mm of cumulative displacement, inset 3; 18.5% at 100 mm of cumulative displacement, inset 4; 20.1% at 60 mm of cumulative displacement, inset 5). The large amplitude of the OFD ratio at the fault stage can be explained by the noise in our experiments as well as by the non-cohesive property of the material which results in thick fault strands.

For the profile located across a future relay zone (Fig. 7), the OFD ratio slightly increases (53%) at the end of the Riedel stage right before the  $R_L$  shears formation (interaction stage). At the beginning of the fault stage, since the Riedel evolves as a relay zone, the OFD ratio strongly increases from 45 to 87.4% (inset 3). Once the relay zone is progressively abandoned, the OFD ratio decreases to reach stable value ranging from 25% to 13.5% with an average of 19.4%.

The Fig. 8 shows the evolution of the average OFD ratio for experiments with different thicknesses and different deposit methods. Since the width of the diffuse deformation zone depends on the sand thickness, the localization on Riedels and the formation of fault strands require more displacement for thicker experiments. As a consequence, we here show the evolution of the average OFD ratio as a function of the applied displacement normalized by the material thickness. We observe the same evolution independently of the sand thickness: 100 to 90% OFD at the initiation stage, an abrupt decrease when the deformation localizes

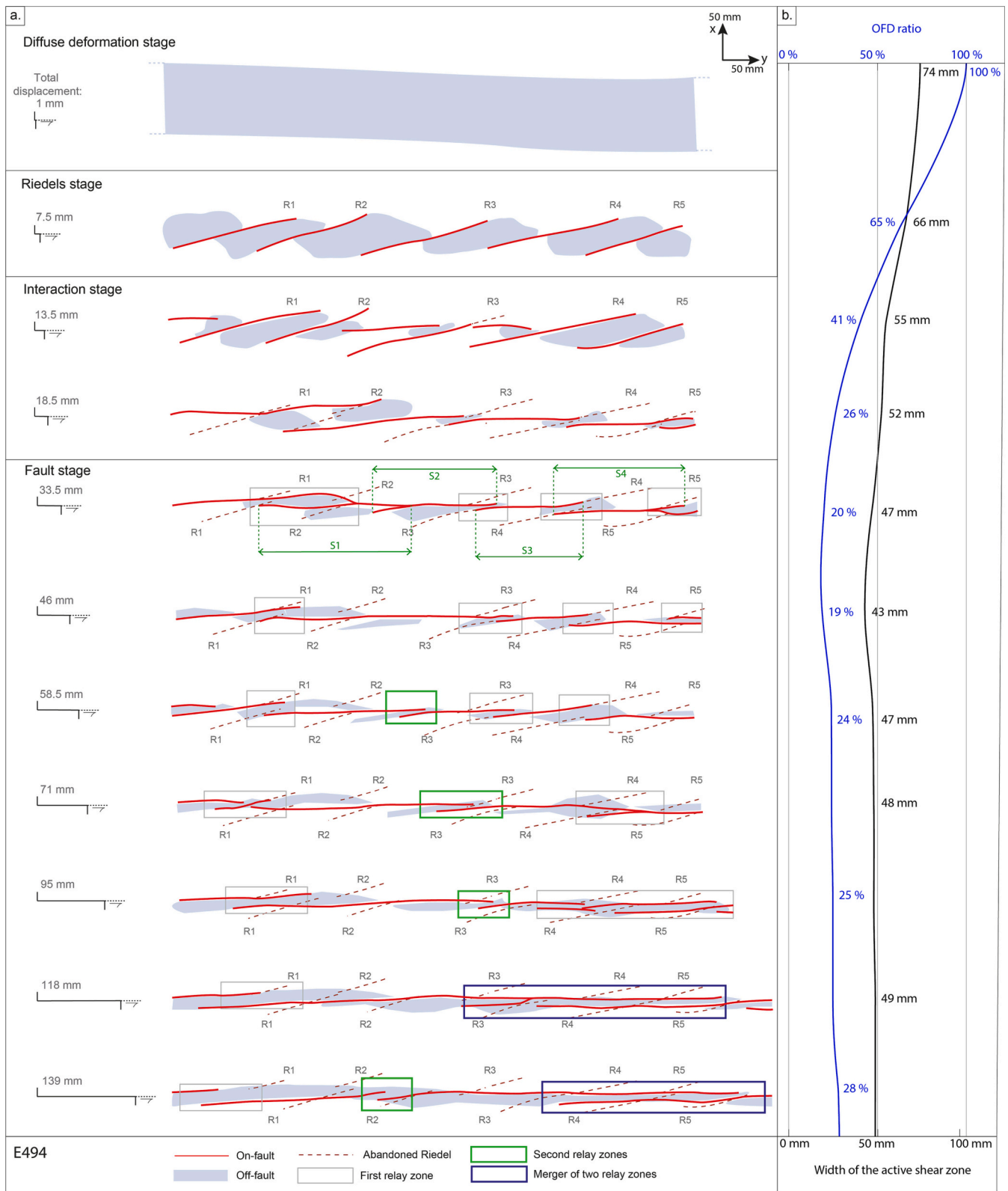


**Fig. 5.** (a) Scheme of the structural evolution of the on- and off-fault deformation with increasing cumulative displacement (from 1 to 139 mm) for a 60 mm thick sand (E494). The red lines represent on-fault deformation, the blue areas the OFD, and the red dashed lines abandoned Riedels. The gray rectangles show the first relay zones appearing during the fault zone formation. The green rectangles represent the second family of relay zones located at fault strand terminations. The blue rectangles represent the fusion of two relay zones. (b) Evolution of the OFD ratio and of the shear zone width during the strike-slip fault evolution.

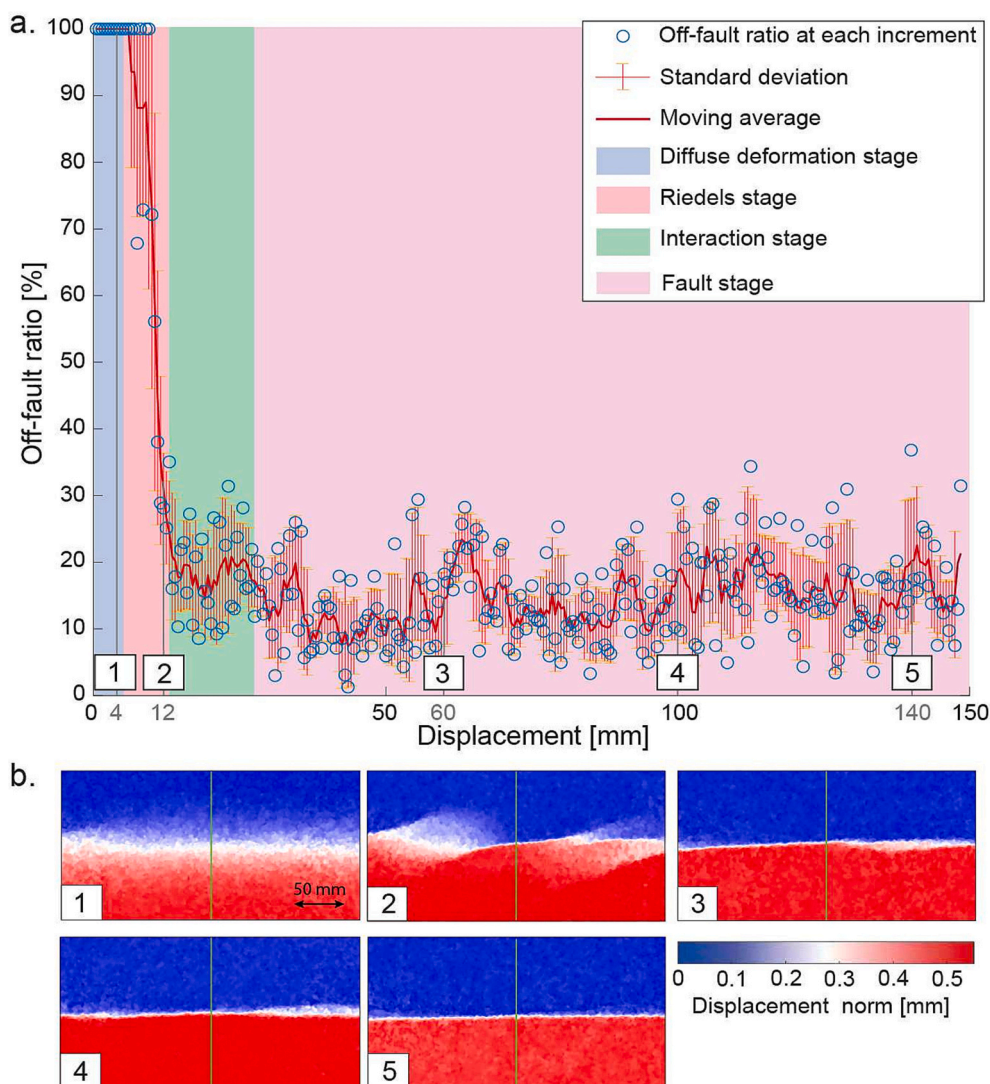


**Fig. 6.** (a) Evolution of the OFD ratio in experiment E484, along a single perpendicular profile crossing a fault strand. (b) Maps of the horizontal displacement norm at different stages of the strike-slip fault formation, and location of the profile (green line) shown in (a).

along the shears, to finally reach a stable value at an average to 22.3% after a normalized cumulative displacement of 0.6 for the poured sand. A slight progressive increase to an average of 26.6% is then observed. This is explained by the continuous reorganization of the relay zones (passive displacement, abandonment and formation of new relay zones) which contributes to maintain a non-negligible residual OFD (see Fig. 5). Since the sedimented sand is more compact and of higher static (or initial) friction than the poured sand, its diffuse deformation phase is longer and its surface deformation appears 0.4 normalized displacement later. However, the same evolution is observed and the internal friction has no influence on the proportion of OFD at the strike-slip fault stage.

### 3.4. 3D mapping of the evolution of off-fault deformation

We carefully investigated patterns of the OFD, at different stages of the strike-slip fault formation, to understand its distribution. The analysis is done across one Riedel shear (size of the zoom is  $225 \times 97$  mm). We show the horizontal displacement norm (Eq. (1), Fig. 9-a), the OFD (Fig. 9-b), the divergence (Eq. (2), Fig. 9-c), the curl (Eq. (3), Fig. 9-d), the vertical displacement generated by 2 mm of applied displacement (Fig. 9-e) and the total (or cumulative) vertical displacement (Fig. 9-f).

In Fig. 9, after 2 mm of displacement, the initial diffuse deformation zone is marked by a positive divergence (Fig. 9c.1) over the entire width

and a maximum cumulative uplift of 0.4 mm (Fig. 9e.1 and f.1). At this stage, the curl does not reveal any rotation of shear bands (Fig. 9d.1). After 8.5 mm of displacement, the deformation is both localized and diffuse: localized deformation along Riedel shears corresponding to the on-fault deformation, and diffuse deformation on both sides and at the extremities of the Riedel (Fig. 9a.2 and b.2). Fig. 9c.2 and e.2 show that positive divergence and uplift dominate (maximum cumulative elevation of 1.2 mm, Fig. 9f.2). On the contrary, there are negative divergence and curl along the Riedels (Fig. 9c.2 and d.2). At 12.5 mm, we observe the same distribution: the Riedel and  $R_L$  are active faults (Fig. 9a.3 and b.3) and the diffuse deformation occurs between them and at their extremities. Similarly, the diffuse deformation is associated with positive divergence and uplift (maximum cumulative elevation of 2.2 mm, Fig. 9c.3, f.3 and d.3) while the on-fault deformation is associated with negative divergence and curl (Fig. 9c.3 and e.3). At 30 mm, the relay zone corresponds to an uplift and positive divergence associated with the OFD (Fig. 9b.4, c.4 and e.4). At this stage, the Riedel is progressively abandoned, and both sides are passively translated while the  $R_L$  propagates. At 75 mm, once the two parts of the Riedel get far enough, so that they do not interact with each other, all the shear bands finally coalesce to form the strike-slip fault, composed of three fault strands, not visible on this zoomed image (Fig. 9a.5). The OFD is distributed along these fault strands and between them, the maximum cumulative elevation is

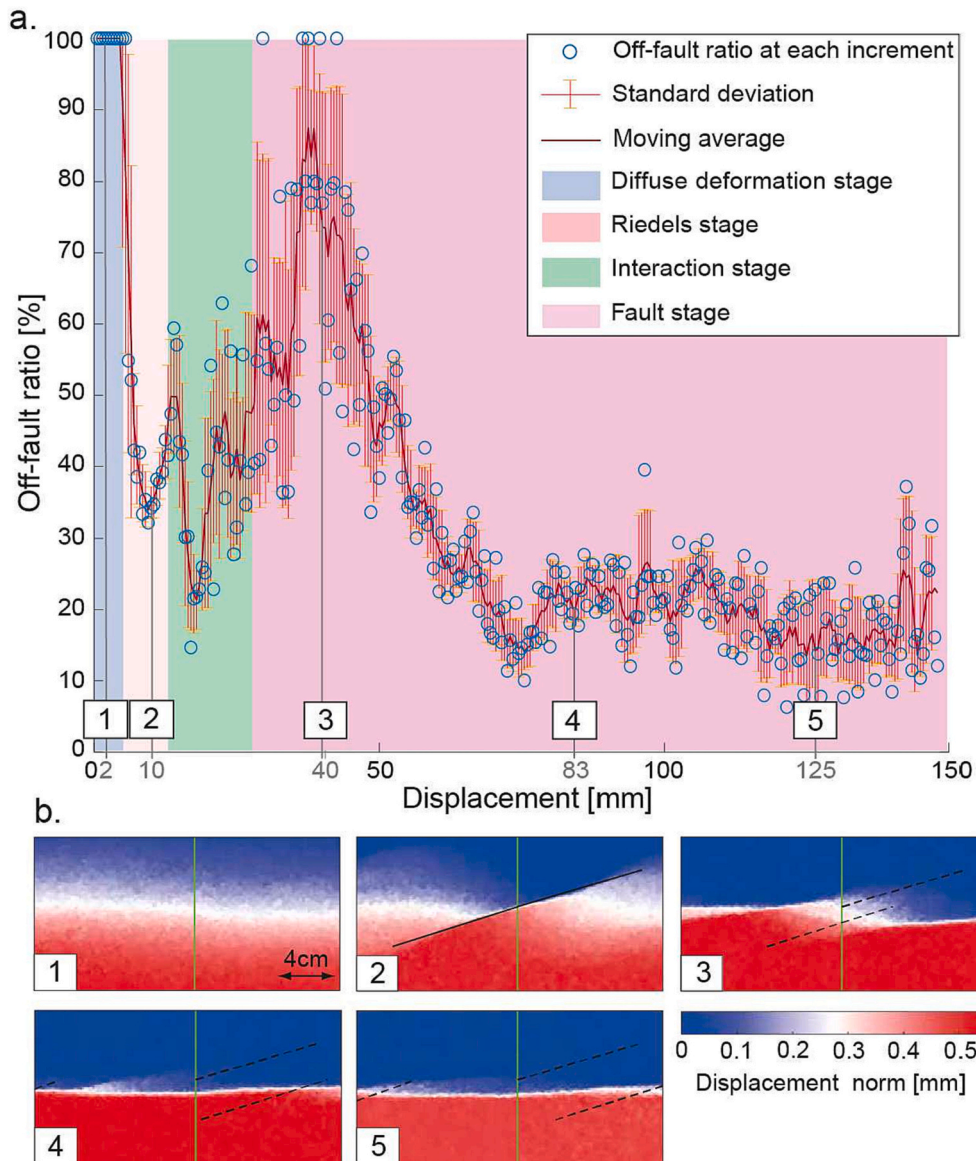


**Fig. 7.** (a) Evolution of the OFD ratio in experiment E481, along a profile perpendicular to the basal fault crossing a relay zone. (b) Maps of the horizontal displacement norm, with the location of the profile (green line) at different stages of the strike-slip fault formation. The black dashed lines represent the inactive Riedels.

of 7 mm (Fig. 9b.5 and f.5).

Since OFD is always associated to an uplift of the sand surface, elevation appears as a good marker of OFD in sandbox experiments. Indeed we observe mainly swelling relay zones in our experiments. Schrank et al. (2008) showed that the degree of compaction of the sand has an influence on the type of topography and could control the fault network structure along strike slip faults in sedimentary basins. We observe the same behavior within our experiments: experiments with sedimented sand have a greater vertical displacement than those with poured sand. Thus while we are probably overestimating the elevation in our sandbox experiments, the fault damage zone is correlated with increase of altitude and is necessarily impacted by the properties of the sand as the initial compaction.

#### 4. Discussion

These analogous experiments with a homogeneous, granular, frictional material such as sand with a linear, non-dilatant basal fault at its base show that the distribution of on- and off-fault deformation along a

strike-slip fault is complex and strongly influenced by the initial Riedels and the following shear bands. The Riedels geometry is itself controlled by the diffuse deformation zone that develops very early in the history of the fault zone and that will limit the length of the Riedels. In this section, we discuss the impact of the initial diffuse deformation zone on the fault zone history, the segmentation of strike-slip faults and the distribution of OFD controlled by these inherited shear bands. We finally compare our results to field and geodetic observations.

##### 4.1. Impact of the initial diffuse deformation zone on the fault zone history

For all experiments, regardless of the internal friction of the sand, the initial stage shows the formation of a diffuse deformation zone that emanates from the basal fault and forms a bulge on the surface. The width of this zone varies according to the thickness and coefficient of internal friction of the sand, the greater the thickness the wider the zone and the greater the coefficient of internal friction the wider the zone (Lefevre et al., 2020; Hatem et al., 2017). This diffuse deformation is

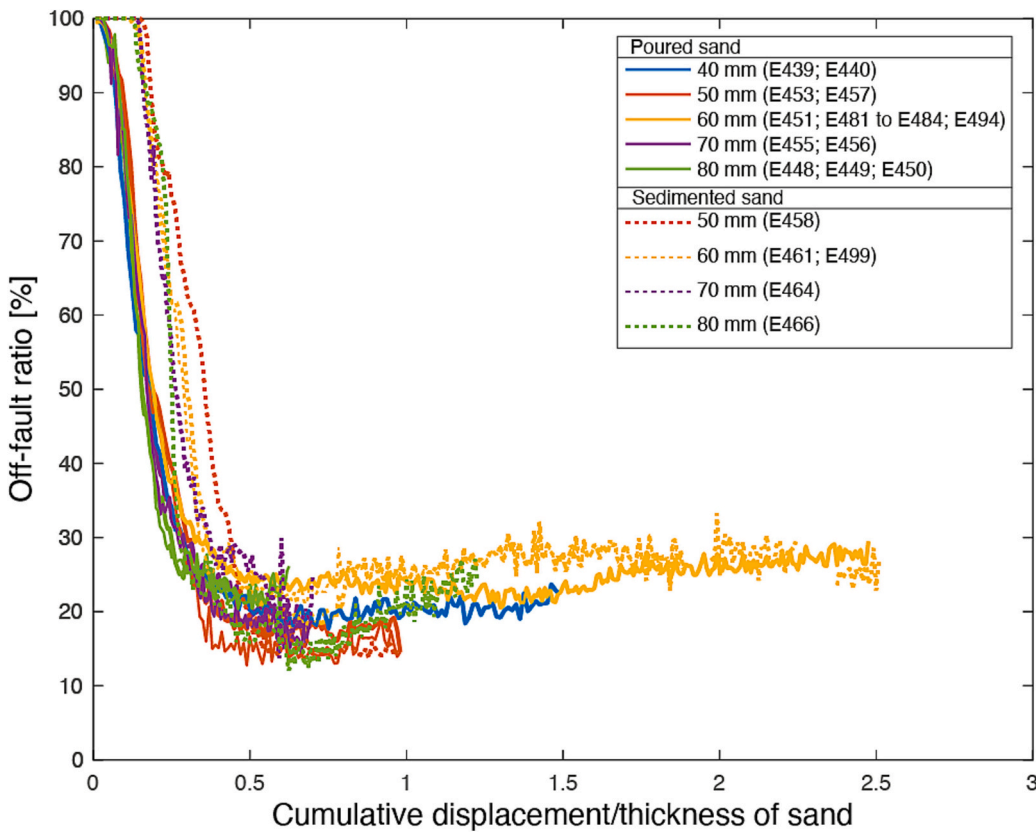


**Fig. 8.** Averaged evolution of the OFD ratio for the twenty experiments (Table 1) as a function of applied displacement normalized by sand thickness. The thickness of the sand pack ranges from 40 to 80 mm. The experiments with manually poured sand are represented by the solid curves, and the experiments using sedimented sand are represented by the dashed curves. Some of the experiments have 50 mm of total applied displacement, and some 150 mm. The OFD evolves similarly for all the experiments. Experiments with the same parameters (sand thickness and deposition method) are averaged and represented with a single curve.

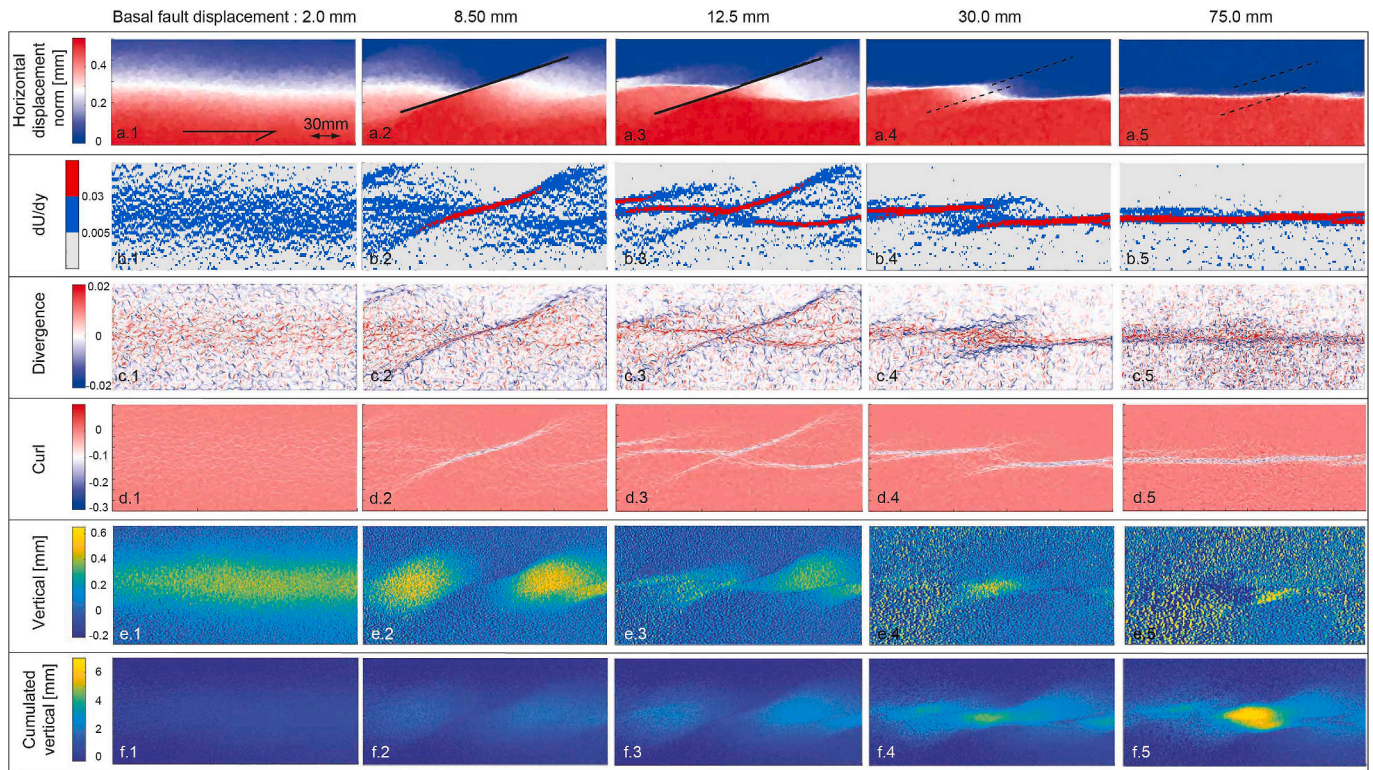


**Fig. 9.** Map view of the evolution of a relay zone (experiment E481, Table 1). The relay zone formed at the intersection between the Riedel and the  $R_L$  is progressively abandoned as the Riedel splits into two parts cut by the through-going fault. (a) Norm of the horizontal displacement between two images cumulating 0.5 mm of applied displacement. Active and abandoned Riedels are represented by black solid and dashed lines, respectively. (b) Off- (blue) and on- (red) fault deformation criterion, (c) Divergence, (d) Curl, (e) Vertical displacement cumulating 2 mm of applied displacement. (f) Cumulative vertical displacement.

amplified by the dilatant properties of the sand and may not be as important on the field. Yet, according to field and geodetic observations, diffuse deformation develops over a large area at the early-stage strike-slip fault, which may be found around the ‘mature’ fault zone as a relic, and which would be abandoned with the progressive localization of deformation on the main fault strand (Frost et al., 2009). Our experimental observations confirm that the width of the diffuse zone delimits the location of the on- and off-fault deformation throughout the experiment and that no deformation occurs beyond this zone. The width of the fault zone is maximum at the initial stage of the strike-slip fault. This width will progressively decrease in the same way as the OFD ratio, until it reaches a minimum value at the beginning of the fault stage, and then increase slightly to reach a stable value until the end of the experiment. The progressive decrease of the fault width is also observed in normal fault analogue models, as shown in the high resolution observations of Mayolle et al. (2021).

#### 4.2. Strike-slip fault structure and OFD distribution controlled by inherited structures

The Fig. 10 summarizes the distribution and the evolution of fault strands, relay zones and OFD zones in six steps. Before the formation of the strike-slip fault at the surface, the structure is expressed by alternating Riedels and OFD zones (Fig. 10-1). The width of the OFD corresponds to the initial diffuse deformation zone, and the amount is of 60–40%. The Riedels are then progressively abandoned in favor of the  $R_L$  shears (Fig. 10-1 and 2). These new shear bands form in between the Riedels. Their tips are parallel to the Riedels but do not seem to branch on them. The OFD takes place at these Riedels and  $R_L$  shears junctions. The overall amount of OFD decreases from 30% to 25%. As displacement continues,  $R_L$  shears rotate to become parallel to the basal fault (Fig. 10-3), decreasing the width and amount of the OFD. These shear bands will form the future fault strands. Former Riedels are sheared, forming the first relay zones. Once the two branches of the Riedels stop interacting, the fault strands cuts through the relay zone, increasing its length (Fig. 10-4). The inactive relay zone is then passively transported, but some OFD remains along these past structures. As the displacement increases, the length of the fault strands increases until the long fault strands become unstable. Once the fault strands reach a certain critical length, a new relay zone forms, at a former Riedel by softening the

structure or shear band location characterized by a remanent OFD (Fig. 10-5).

The formation of these new relay zones leads to a permanent alteration of fault strands and relay zones (Fig. 10-6). Throughout these 6 stages, the OFD is systematically associated with uplift and positive divergence.

Hence, the main results are as follows: (1) The structure of the fault zone is acquired very early in the history of the strike-slip fault and is largely controlled by the Riedels and the width of the diffuse zone at the first stage of the fault, i.e. the initial thickness of the sand. (2) OFD is systematically located at these relay zones and along past shear bands. (3) The fault zone and hence OFD width decrease with the cumulative displacement, to reach a minimum value before a slight progressive increase to a stable value. Similarly, the amount of OFD decreases with the cumulative displacement to reach a minimum of 22.3% before a slight progressive increase to 26.6%. (4) Uplift is a good marker of OFD zones.

#### 4.3. Comparison with observations in a natural context

Our analogue experiments are consistent with studies suggesting that the length of fault strands scales with the thickness of the seismogenic crust (Bilham and Williams, 1985; Klinger, 2010; Lefevre et al., 2020). Segments develop between Riedels, the distance of which is controlled by the thickness of the material (Lefevre et al., 2020). Segments then connect when relay zones are abandoned to form fault strands. New relay zones can appear throughout the evolution of the strike-slip fault, in particular when the fault strand reaches a certain threshold.

Both field and geodetic observations and sandbox experiments show that the OFD is mainly located along geometric complexities (Dolan and Haravitch, 2014; Antoine et al., 2021). Here we show a qualitative comparison between relay zones of an earthquake rupture and those observed in our experiments (Fig. 11). We selected two relay zones of the 2013 Mw 7.7 Balochistan earthquake in Pakistan (calculated by Antoine et al., 2022), which ruptured the 200 km-long senestral Hoshab fault (Fig. 11-b and c). Horizontal and vertical displacements and curl in the experiments and this natural example show similar patterns. On the C2 relay, as on the E481 relay, we observe two parallel main fault strands, which accommodate negative rotation (clockwise), and delimit a more diffuse deformation zone, which accommodates an uplift. On the

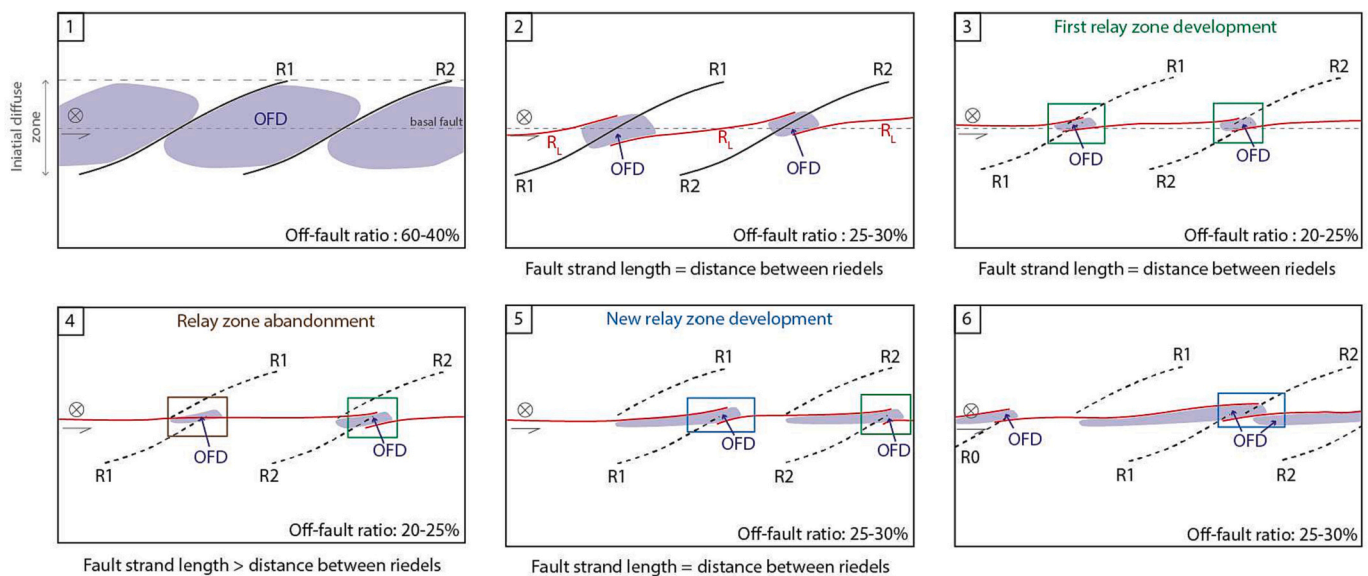


**Fig. 10.** Summary of the spatial distribution and evolution of the fault zone and the OFD areas. Solid lines represent active fault strands. Dashed lines represent inactive ones. The squares locate the relay zones, green: the first relay zones, brown: abandoned relay zones, blue: newly formed relay zones. Numbers 1 to 6 correspond to increasing applied displacement.

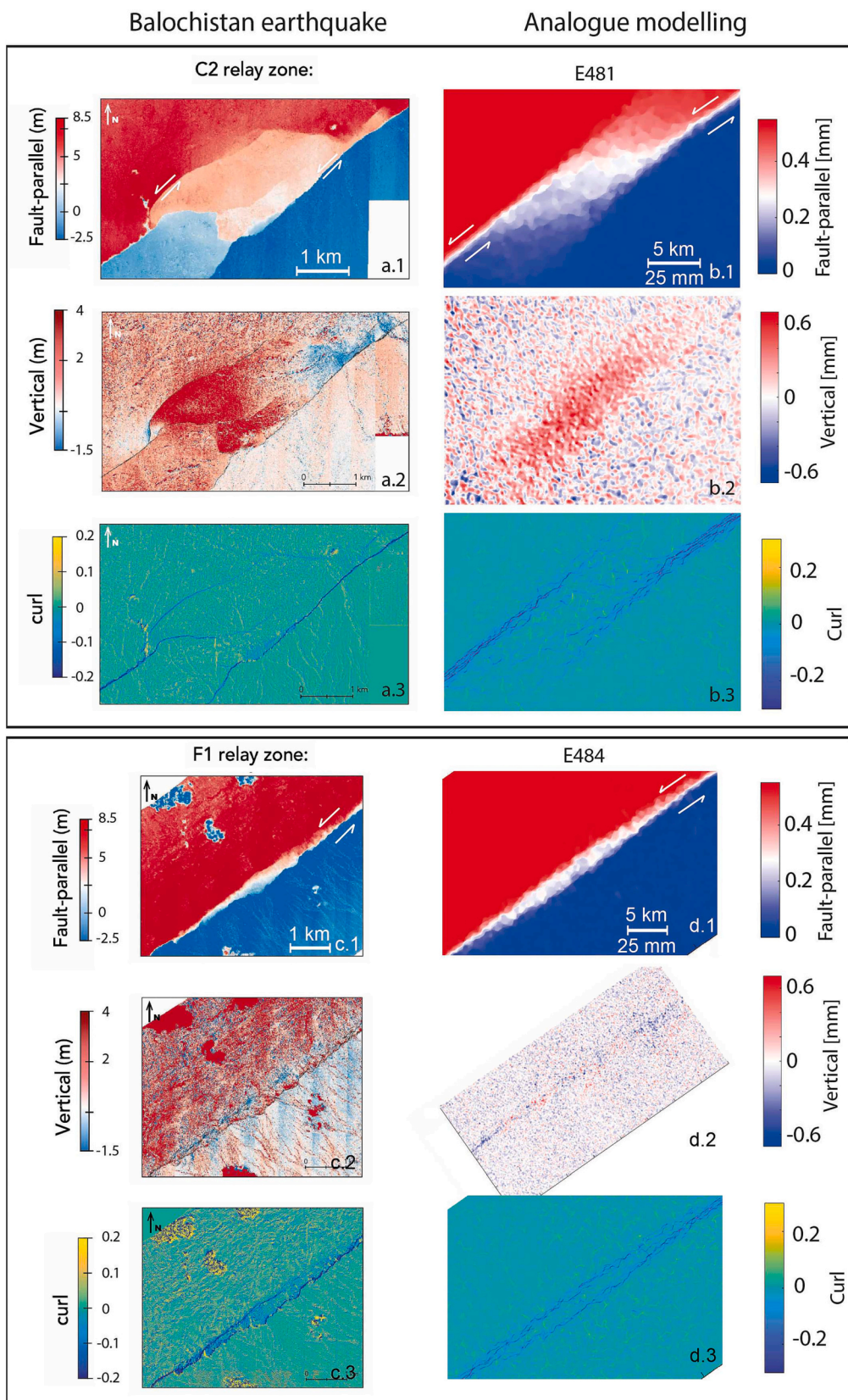


**Fig. 11.** Co-seismic displacements and curl maps of two relay zones of the 2013 Mw 7.7 Balochistan earthquake in Pakistan (columns a and c, calculated with the MicMac open-source photogrammetry software with WorldView and Pléiades images to measure the 3D high-resolution (0.5 m) near-fault surface displacement, Antoine et al., 2022), compared with two relay zones of experiments E481 (column b) and E484 (column d). Lengths were scaled with  $L^*$ . The first line shows the horizontal displacement parallel to the fault, the second line the vertical displacement and the third line the curl.

F1 relay, like the relay in experiment E484, we also observe two fault strands, here closer together, which also delimit a more diffuse deformation zone. These common features indicate a similar behaviour between the crustal faults and the experimental strike-slip faults. However, we can observe some differences. In particular, the C2 relay zone in the Balochistan has two secondary fault strands that connect the main fault strands and that are not found in the E481 relay zone. Another difference is the near absence of vertical motion in the E484 relay zone, while it is not observed in the F1 relay zone of the Balochistan, perhaps explained by the reverse component of the Balochistan earthquake, which does not exist in our experiments. The very simple character of the analogue models and their finite length do not allow for a perfect similarity with the field examples, and this is not the aim. The objective is to understand certain behaviour by simplifying a process.

The seismogenic crust of the Balochistan, located in the Pakistani Makran, where the 2013 earthquake occurred, has a thickness of 10 to 18 km (Lauer et al., 2020). The experiment used to compare the model to nature has a thickness of 60 mm which corresponds to 12 km, considering the scaling ( $L^* = 0.5 \times 10^{-5}$ ). When we scale the displacement maps of the experiments with  $L^*$ , the structures of the models are five times larger than in nature. This difference may be related to the granular nature of the sand as well as its homogeneity and the absence of inherited structures.

Our experiments are also consistent with studies suggesting that the width of the fault zone and its geometric complexities decrease with cumulative displacement (Wesnousky, 1988; Stirling et al., 1996; Dolan and Haravitch, 2014; Manighetti et al., 2021), although the number of complexities, controlled by the initial fault strands length, is constant (Manighetti et al., 2021). As the width of geometric complexities decreases with fault maturity, the width and quantity of the OFD also decrease (Dolan and Haravitch, 2014; Gold et al., 2015; Milliner et al., 2020). In our experiments, the OFD ratio varies from 100 to 20% in the early stages of the fault zone formation (from 0 to about 40 mm

displacement, i.e. 0 to 1 times the material thickness) to reach a stable value with an average of 22.3% before a slight gradual increase to 26.6% (from 40 to 150 mm displacement, 1 to 5 times the material thickness) (Figs. 8 and 12). This conclusion is also shared by Hatem et al. (2017), who showed that the OFD in their experiments with wet kaolin seems to stabilize once the slip fault has reached a through-going fault stage.

Fig. 12 shows the evolution of the OFD as a function of increasing cumulative displacement for both analogue experiments and field or geodetic measurements. This comparison requires to take into account the different methods used by the authors to quantify the OFD. For earthquake not captured by satellite (Rockwell et al., 2002), OFD was measured using field methods. In most studies, the OFD ratio was obtained from the deduction of the on-fault deformation (measured either directly in the field or by optical image correlation) from the total deformation measured by image correlation (Zinke et al., 2014, 2019; Milliner et al., 2015, 2020; Gold et al., 2015; Antoine et al., 2021). In some studies, on-fault deformation is either defined as the trace of all major fault strands (Milliner et al., 2015; Zinke et al., 2019), or as a more or less wide area around the main fault strand (Gold et al., 2015; Antoine et al., 2021). Furthermore, the total deformation (i.e. away from the main fault) is also subject to discussion, the larger the study area the more large-scale deformation can be taken into account without any relationship with the OFD.

Quantifications range from 56% OFD (Ridgecrest, Milliner et al., 2020, Balochistan, Zinke et al., 2019) for faults accumulating the lowest amount of cumulated displacement to 15% OFD (Izmit and Duzce, 1997, Rockwell et al., 2002) on faults with the largest cumulative displacement. Dolan and Haravitch (2014) define a “surface slip ratio” (SSR) as the ratio of mean surface slip on the fault to average slip at 3–6 km depth, which they associate with the OFD (the higher the SSR the less OFD and vice versa). They proposed that OFD reaches a stable value after about 100 km of cumulative displacement with a OFD ratio varying from 15 to 20% (Izmit, Denali, Kunlun).

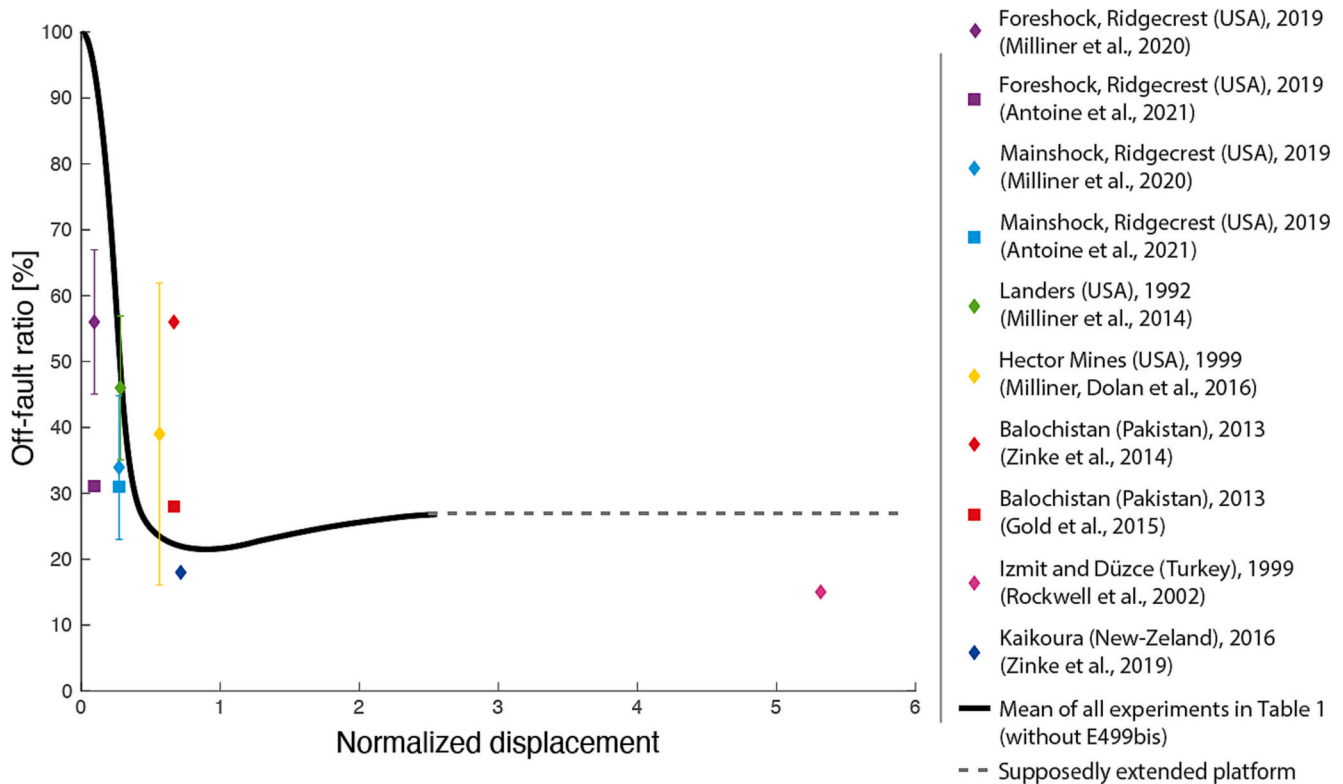


Fig. 12. Average evolution of the OFD ratio as a function of the cumulative displacement normalized by crust thickness for natural examples and material thickness for the experiments. The black curve represents the mean ratio for all experiments described in Table 1. The coloured dots of different shapes represent the OFD ratio for different earthquakes for which the OFD has been estimated.

Our models also show high OFD ratios in the early stages of strike-slip faulting, i.e. at small cumulative displacements, followed by a rapid decrease in ratio to finally reach a stable value. This comparison might however be affected by four major differences. Firstly, most of the field and geodetic observations estimates were made for active faults. The first difference is therefore the use of frictional materials that are very stiff and without measurable stick-slip properties. The sand being very stiff is not scaled for elasticity, so there is not enough elastic deformation to obtain a seismic cycle, i.e. an inter-seismic period where the fault is locked with an accumulation of elastic deformation followed by a seismic event that releases the accumulated elastic stress. The second difference is the choice of a linear, zero width basal fault. [Hatem et al. \(2017\)](#) describe a higher fault zone complexity in their experiments for wide basal faults (15 mm). They also suggest that the depth of the basal fault has an impact on the complexity of the fault zone and therefore the amount of OFD. In our sand models, the greater the material thickness the later the OFD stable value at 22.3% is reached, but once on the stable value, the amount of OFD no longer varies with sand thickness (from 20 mm to 40 mm, [Fig. 8](#)). Another difference is the initial homogeneity of the sand package, whereas the real faults develop in a heterogeneous crust with inherited structures. This inheritance most likely increases the amount of OFD. In particular, some studies have shown that weaker near-surface materials tend to increase the OFD ([Zinke et al., 2019](#)).

Nevertheless, our models confirm the existence of an OFD stable value but with a slightly higher proportion of OFD ratio from 22.3% to 26.6%. This difference can be explained by the non-cohesive nature of the sand. In nature, the on-fault deformation is characterized by a localized displacement over a very narrow rupture zone. In our experiments the sand is not cohesive, the rupture is characterized by a shear zone, thus less sharp on the fault. The gradient of the displacement norm is therefore less localized than in nature and includes a small proportion of OFD that is not found in the field.

## 5. Conclusion

We document the evolution of OFD during the formation and evolution of laboratory strike-slip faults. A strike-slip fault forms in four main stages. During these four stages the amount of OFD varies from 100% at the initiation stage to a stable value at 22.3% when the fault zone is completely formed before a slight progressive increase to 26.6%, due to the expansion of the fault's damage zone. OFD is mainly concentrated in structurally complex zones, acting as relay zones. Our models show that the location of these relay zones is imposed very early in the history of the fault zone since it is controlled by the location of the Riedels, which are the first faults to appear at the surface. Moreover, after a significant amount of cumulative displacement, the fault zone, which could be described as "mature" when compared to natural examples, is composed of alternating relay zones and fault strands. The length of the fault strands is controlled by the initial inter-Riedel distance. During the fault zone evolution, the relay zones are consecutively active, abandoned and passively translated, and finally re-formed. Our models also show that beyond a certain length, the fault strands break in two over old complexities (Riedels or abandoned relay zones) to recover a lower length. This suggests that strike-slip faults will never reach a continuous, linear geometry even if linear at depth.

However, field measurements are usually acquired after earthquakes, whereas, in our study, OFD is measured throughout the evolution of a fault zone. In order to obtain a better quantification of the OFD in the laboratory, it would therefore be interesting to use a stick-slip material.

## CRedit authorship contribution statement

**Sarah Visage:** Conceptualization, Methodology, Formal-analysis, Writing-original-draft, Writing-review-editing, Visualization. **Pauline**

**Souloumiac:** Conceptualization, Methodology, Writing-original-draft, Writing-review-editing, Supervision. **Nadaya Cubas:** Conceptualization, Writing-original-draft, Writing-review-editing, Supervision. **Bertrand Maillot:** Conceptualization, Methodology, Writing-original-draft, Writing-review-editing, Supervision. **Solene Antoine:** Conceptualization, Visualization, Writing-review-editing. **Arthur Delorme:** Software, Writing-review-editing. **Yann Klinger:** Conceptualization, Writing-review-editing, Funding-acquisition.

## Declaration of Competing Interest

The authors declare that they have no known competing financial interests or personal relationships that could have appeared to influence the work reported in this paper.

## Data availability

Heavy data but can be provided on request.

## Acknowledgments

We thank Baptiste Mary, Ewelina Rupnik and Marc Pierrot-Deseilligny for their precious help in using and optimising the Micmac software and Bastien Roucariés for the development of the step motor of the experimental box. We thank Fabrizio Storti and Stéphane Dominguez for their helpful reviews. This work has been partially funded by the French National Research Agency (ANR, France) in the framework of the Disrupt project (ANR-18-CE31-0012) and by the Initiative of Excellence of CY Cergy Paris Université.

## References

- Antoine, S., Klinger, Y., Delorme, A., Gold, R.D., 2022. Off-fault deformation in regions of complex fault geometries: The 2013, mw7.7, baluchistan rupture (Pakistan). *J. Geophys. Res.: Solid Earth*, e2022JB024480.
- Antoine, S.L., Klinger, Y., Delorme, A., Wang, K., Bürgmann, R., Gold, R.D., 2021. Diffuse deformation and surface faulting distribution from submetric image correlation along the 2019 Ridgecrest, California, ruptures. *Bull. Seismol. Soc. Am.*
- Baize, S., Nurminen, F., Sarmiento, A., Dawson, T., Takao, M., Scotti, O., Azuma, T., Boncio, P., Champenois, J., Cinti, F.R., et al., 2020. A worldwide and unified database of surface ruptures (sure) for fault displacement hazard analyses. *Seismol. Res. Lett.* 91 (1), 499–520.
- Bilham, R., Williams, P., 1985. Sawtooth segmentation and deformation processes on the southern san andreas fault, California. *Geophys. Res. Lett.* 12 (9), 557–560.
- Choi, J.-H., Klinger, Y., Ferry, M., Ritz, J.-F., Kurtz, R., Rizza, M., Bollinger, L., Davaasambuu, B., Tsend-Ayush, N., Demberel, S., 2018. Geologic inheritance and earthquake rupture processes: The 1905 m  $\geq$  8 tsetserleg-bulnay strike-slip earthquake sequence, Mongolia. *J. Geophys. Res.: Solid Earth* 123 (2), 1925–1953.
- Cubas, N., Maillot, B., Barnes, C., 2010. Statistical analysis of an experimental compressional sand wedge. *J. Struct. Geol.* 32 (6), 818–831.
- Delorme, A., Grandin, R., Klinger, Y., Pierrot-Deseilligny, M., Feuillet, N., Jacques, E., Rupnik, E., Morishita, Y., 2020. Complex deformation at shallow depth during the 30 october 2016 mw6.5 norcia earthquake: interference between tectonic and gravity processes? *Tectonics* 39 (2), e2019TC005596.
- Dolan, J.F., Haravitch, B.D., 2014. How well do surface slip measurements track slip at depth in large strike-slip earthquakes? The importance of fault structural maturity in controlling on-fault slip versus off-fault surface deformation. *Earth Planet. Sci. Lett.* 388, 38–47.
- Dooley, T.P., Schreurs, G., 2012. Analogue modelling of intraplate strike-slip tectonics: A review and new experimental results. *Tectonophysics* 574, 1–71.
- Dunham, E.M., Kozdon, J.E., Belanger, D., Cong, L., 2011. Earthquake ruptures on rough faults. In: *Multiscale and multiphysics processes in geomechanics*. Springer, pp. 145–148.
- Frost, E., Dolan, J., Sammis, C., Hacker, B., Cole, J., Ratschbacher, L., 2009. Progressive strain localization in a major strike-slip fault exhumed from midseismogenic depths: Structural observations from the salzach-ennstal-mariazell-puchberg fault system, Austria. *J. Geophys. Res.: Solid Earth* 114 (B4).
- Gabriel, A.-A., Ampuero, J.-P., Dalguer, L., Mai, P.M., 2013. Source properties of dynamic rupture pulses with off-fault plasticity. *J. Geophys. Res.: Solid Earth* 118 (8), 4117–4126.

- Galland, O., Bertelsen, H.S., Guldstrand, F., Girod, L., Johannessen, R.F., Bjugger, F., Burchardt, S., Mair, K., 2016. Application of open-source photogrammetric software micmac for monitoring surface deformation in laboratory models. *J. Geophys. Res.: Solid Earth* 121 (4), 2852–2872.
- Gold, R.D., Reitman, N.G., Briggs, R.W., Barnhart, W.D., Hayes, G.P., Wilson, E., 2015. On- and off-fault deformation associated with the September 2013 Mw 7.7 Balochistan earthquake: Implications for geologic slip rate measurements. *Tectonophysics* 660 (September 2013), 65–78.
- Hatem, A.E., Cooke, M.L., Toeneboehn, K., 2017. Strain localization and evolving kinematic efficiency of initiating strike-slip faults within wet kaolin experiments. *J. Struct. Geol.* 101, 96–108.
- Jiao, L., Klinger, Y., Scholtes, L., 2021. Fault segmentation pattern controlled by thickness of brittle crust. *Geophys. Res. Lett.* 48 (19), e2021GL093390.
- King, G., Nábělek, J., 1985. Role of fault bends in the initiation and termination of earthquake rupture. *Science* 228 (4702), 984–987.
- Klinger, Y., 2010. Relation between continental strike-slip earthquake segmentation and thickness of the crust. *J. Geophys. Res.: Solid Earth* 115 (B7).
- Klinger, Y., Michel, R., King, G., 2006. Evidence for an earthquake barrier model from mw 7.8 kokoxili (tibet) earthquake slip-distribution. *Earth Planet. Sci. Lett.* 242 (3–4), 354–364.
- Klinger, Y., Okubo, K., Vallage, A., Champenois, J., Delorme, A., Rougier, E., Lei, Z., Knight, E.E., Munjiza, A., Satriano, C., et al., 2018. Earthquake damage patterns resolve complex rupture processes. *Geophys. Res. Lett.* 45 (19), 10–279.
- Klinger, Y., Xu, X., Tapponnier, P., Van der Woerd, J., Lasserre, C., King, G., 2005. High-resolution satellite imagery mapping of the surface rupture and slip distribution of the m w 7.8, 14 november 2001 Kokoxili earthquake, Kunlun fault, Northern Tibet, China. *Bull. Seismol. Soc. Am.* 95 (5), 1970–1987.
- Klinkmüller, M., Schreurs, G., Rosenau, M., Kemnitz, H., 2016. Properties of granular analogue model materials: A community wide survey. *Tectonophysics* 684, 23–38.
- Lauer, B., Grandin, R., Klinger, Y., 2020. Fault geometry and slip distribution of the 2013 mw 7.7 balochistan earthquake from inversions of sar and optical data. *J. Geophys. Res.: Solid Earth* 125 (7), e2019JB018380.
- Lefevre, M., Souloumiac, P., Cubas, N., Klinger, Y., 2020. Experimental evidence for crustal control over seismic fault segmentation. *Geology* 48 (8), 844–848.
- Maillet, B., 2013. A sedimentation device to produce uniform sand packs. *Tectonophysics* 593, 85–94.
- Manighetti, I., Campillo, M., Bouley, S., Cotton, F., 2007. Earthquake scaling, fault segmentation, and structural maturity. *Earth Planet. Sci. Lett.* 253 (3–4), 429–438.
- Manighetti, I., Mercier, A., De Barros, L., 2021. Fault trace corrugation and segmentation as a measure of fault structural maturity. *Geophys. Res. Lett.* 48 (20), e2021GL095372.
- Mayolle, S., Soliva, R., Dominguez, S., Wibberley, C., Caniven, Y., 2021. Nonlinear fault damage zone scaling revealed through analog modeling. *Geology* 49 (8), 968–972.
- McGill, S.F., Rubin, C.M., 1999. Surficial slip distribution on the central emerson fault during the june 28, 1992, landers earthquake, California. *J. Geophys. Res.: Solid Earth* 104 (B3), 4811–4833.
- Milliner, C., Dolan, J., Hollingsworth, J., Leprince, S., Ayoub, F., 2016. Comparison of coseismic near-field and off-fault surface deformation patterns of the 1992 mw 7.3 landers and 1999 mw 7.1 hector mine earthquakes: Implications for controls on the distribution of surface strain. *Geophys. Res. Lett.* 43 (19), 10–115.
- Milliner, C., Donnellan, A., Aati, S., Avouac, J.-P., Zinke, R., Dolan, J.F., Wang, K., Bürgmann, R., 2020. Bookshelf kinematics and the effect of dilatation on fault zone inelastic deformation: Examples from optical image correlation measurements of the 2019 ridgecrest earthquake sequence. *J. Geophys. Res.: Solid Earth*, e2020JB020551.
- Milliner, C.W., Dolan, J.F., Hollingsworth, J., Leprince, S., Ayoub, F., Sammis, C.G., 2015. Quantifying near-field and off-fault deformation patterns of the 1992 mw 7.3 landers earthquake. *Geochem. Geophys. Geosyst.* 16 (5), 1577–1598.
- Naylor, M., Mandl, G., Supestijn, C., 1986. Fault geometries in basement-induced wrench faulting under different initial stress states. *J. Struct. Geol.* 8 (7), 737–752.
- Riedel, W., 1929. Zur mechanik geologischer brucherscheinungen ein beitrag zum problem der fiederspatten. *Zentbl. Miner. Geol. Palaont. Abt.* 354–368.
- Rockwell, T.K., Lindvall, S., Dawson, T., Langridge, R., Lettis, W., Klinger, Y., 2002. Lateral offsets on surveyed cultural features resulting from the 1999 izmit and duzce earthquakes, Turkey. *Bull. Seismol. Soc. Am.* 92 (1), 79–94.
- Rosu, A.-M., Pierrot-Deseilligny, M., Delorme, A., Binet, R., Klinger, Y., 2015. Measurement of ground displacement from optical satellite image correlation using the free open-source software micmac. *ISPRS J. Photogramm. Remote Sens.* 100, 48–59.
- Rupnik, E., Daakir, M., Deseilligny, M.P., 2017. Micmac—a free, open-source solution for photogrammetry. *Open Geospatial Data Software Standards* 2 (1), 1–9.
- Schrank, C.E., Boutelier, D.A., Cruden, A.R., 2008. The analogue shear zone: From rheology to associated geometry. *J. Struct. Geol.* 30 (2), 177–193.
- Schreurs, G., 2003. Fault development and interaction in distributed strike-slip shear zones: an experimental approach. *Geol. Soc. Lond. Spec. Publ.* 210 (1), 35–52.
- Segall, P., Pollard, D., 1980. Mechanics of discontinuous faults. *J. Geophys. Res.: Solid Earth* 85 (B8), 4337–4350.
- Shelef, E., Oskin, M., 2010. Deformation processes adjacent to active faults: Examples from Eastern California. *J. Geophys. Res.: Solid Earth* 115 (B5).
- Stirling, M.W., Wesnousky, S.G., Shimazaki, K., 1996. Fault trace complexity, cumulative slip, and the shape of the magnitude-frequency distribution for strike-slip faults: A global survey. *Geophys. J. Int.* 124 (3), 833–868.
- Tchalenko, J., 1970. Similarities between shear zones of different magnitudes. *Geol. Soc. Am. Bull.* 81 (6), 1625–1640.
- Thomas, M.Y., Bhat, H.S., 2018. Dynamic evolution of off-fault medium during an earthquake: a micromechanics based model. *Geophys. J. Int.* 214 (2), 1267–1280.
- Vallage, A., 2016. Distribution de la déformation en contexte Tectonique oblique: application aux séismes de Denali (2002) et du Balochistan (2013). PhD thesis. Institut de Physique du Globe de Paris.
- Wesnousky, S.G., 1988. Seismological and structural evolution of strike-slip faults. *Nature* 335 (6188), 340–343.
- Wesnousky, S.G., 2006. Predicting the endpoints of earthquake ruptures. *Nature* 444 (7117), 358–360.
- Zinke, R., Hollingsworth, J., Dolan, J.F., 2014. Surface slip and off-fault deformation patterns in the 2013 MW 7.7 Balochistan, Pakistan earthquake: Implications for controls on the distribution of near-surface coseismic slip. *Geochem. Geophys. Geosyst.* 5034–5050.
- Zinke, R., Hollingsworth, J., Dolan, J.F., Van Dissen, R., 2019. Three-dimensional surface deformation in the 2016 mw 7.8 kaikōura, new zealand, earthquake from optical image correlation: Implications for strain localization and long-term evolution of the pacific-australian plate boundary. *Geochem. Geophys. Geosyst.* 20 (3), 1609–1628.